PROCEEDINGS, 51st Workshop on Geothermal Reservoir Engineering
Stanford University, Stanford, California, February 9-11, 2026
SGP-TR-230

New Computational Framework for Fracture-Controlled Reservoir Performance Optimization

Ondřej Pártl[(1)] and Ernesto Meneses Rioseco[(2,3)]

[(1)]Weierstrass Institute for Applied Analysis and Stochastic, Anton-Wilhelm-Amo-Str. 39, 10117, Berlin, Germany

[(2)]Georg-August-Universität Göttingen, Dept. Structural Geology and Geothermics, Goldschmidtstr. 3, D-37077 Göttingen, Germany

[(3)]LIAG-Institute for Applied Geophysics, Dept. Static Modeling, Stilleweg 2, D-30655 Hannover, Germany

partl@wias-berlin.de, ernesto.menesesrioseco@uni-goettingen.de

Keywords: 3D Discrete fracture network modeling; Geothermal well optimization; Geothermal energy production; Immersed boundary method; Non-matching discretization; Well-fracture interaction; Thermo-hydraulic simulation.

ABSTRACT

Fracture-controlled geothermal reservoirs pose significant challenges for numerical simulation and production optimization due to their strong structural heterogeneity and anisotropy. In recent work, we introduced a computational framework that enables efficient optimization of geothermal well configurations in three-dimensional discrete fracture network (DFN) reservoirs without repeated remeshing. In this contribution, we present our most recent methodological advances and numerical results. In particular, we introduce an additional approach for the treatment of well–fracture intersections, aiming at improving robustness and accuracy when production wells intersect fractures under varying inclination and azimuth angles. Furthermore, we report additional verification and validation tests of the proposed framework using generic fracture-controlled reservoir models. These tests focus on the optimization of production well orientation and investigate the influence of well inclination and azimuth on fracture connectivity, pressure response, and thermal performance. The results demonstrate the capability of the framework to reliably capture the impact of well–fracture geometry on reservoir behavior and to identify optimal well placements in simplified but still complex fractured systems. The presented developments represent a further step toward computationally efficient and physically consistent optimization workflows for geothermal reservoir engineering.

1. INTRODUCTION

Fracture-controlled geothermal reservoirs represent one of the most challenging classes of subsurface systems with respect to exploration, characterization, numerical modeling, simulation, and long-term performance forecasting (e.g., Bratton et al. (2006); Vidal & Genter (2018); Patterson et al. (2020)). Their complexity arises from the strong heterogeneity and anisotropy imposed by fracture networks that dominate fluid flow and heat transport, often decoupling hydraulic behavior from matrix properties. Accurately predicting reservoir performance, therefore, requires an integrated understanding of geological structure, fracture topology, thermo-hydraulic processes, and their scale-dependent interactions (e.g., Narr et al. (2006)). These challenges are encountered worldwide in both sedimentary and crystalline geothermal systems and are particularly prominent, for instance, in structurally complex geothermal reservoirs of Europe. Representative examples include the Upper Jurassic carbonate reservoirs of the Greater Munich Region, where productivity is largely controlled in some sectors of the reservoir by fault and fracture zones and in other sectors by matrix permeability, as well as fault damage zones within the Middle Buntsandstein formation in the Upper Rhine Graben, where deformation-related fracture corridors govern permeability enhancement and geothermal potential (e.g., Dussel et al. (2016); Krumbholz et al. (2024); Frey et al. (2022); Bauer et al. (2015)).

To capture the impact of fractures on reservoir behavior, a variety of modeling approaches have been developed over the past decades. Simplified continuum representations, such as the Equivalent Porous Medium (EPM) approach, assume that fracture effects can be upscaled into effective anisotropic permeability tensors, while Dual Porosity Models (DPM) and Dual Porosity Dual Permeability Models (DPDPM) explicitly distinguish between fracture and matrix continua while still relying on volumetric averaging assumptions (Warren & Root (1963); Barenblatt et al. (1960); Gringarten (1982)). More advanced formulations, such as the Embedded Discrete Fracture Model (EDFM), allow fractures to be represented explicitly within a non-conforming matrix grid, significantly reducing meshing complexity compared to fully resolved approaches (Sepehrnoori et al. (2021); Moinfar et al. (2014)). However, for highly heterogeneous and anisotropic fracture-controlled reservoirs, the thermo-hydraulic behavior can only be accurately captured when the geometry, connectivity, and hydraulic properties of individual fractures are explicitly resolved (e.g., Long & Witherspoon (1985)). In this context, Discrete Fracture Network (DFN) models provide the highest level of physical fidelity by representing fractures as explicit lower-dimensional objects embedded in the rock matrix, enabling realistic simulation of flow and heat transport along complex fracture pathways (e.g., Wang et al. (2021); Berre et al. (2019)). Recent studies have demonstrated that DFN-based simulations are essential to reproduce observed production behavior in fractured geothermal reservoirs, particularly under transient thermal loading conditions (e.g., Fadel et al. (2023)).

Beyond accurate forward modeling, the sustainable exploitation of geothermal energy from fracture-controlled reservoirs critically depends on optimal reservoir development strategies (e.g., Salimzadeh et al. (2019); Schulte et al. (2010)). Well placement, spacing, orientation, and operational controls strongly influence thermal breakthrough, reservoir longevity, and overall energy recovery (e.g., Gan & Elsworth (2016)). Optimization of geothermal production, therefore, represents a key research focus, especially in fractured systems where small changes in well positions can result in orders-of-magnitude differences in productivity due to fracture connectivity effects (Glaas et al. (2021); Cao & Sharma (2024); Bödvarsson & Tsang (1982)). In this context, optimization workflows must account for

complex three-dimensional permeability structures, thermo-hydraulic coupling, and long-term sustainability constraints, while remaining computationally feasible.

However, identifying optimal multi-well layouts in three-dimensional, fracture-controlled reservoirs poses severe computational challenges. Traditional numerical approaches often rely on repeated remeshing when sweeping well positions or orientations through the reservoir domain, resulting in prohibitively expensive simulation workflows. To circumvent this bottleneck, the development of efficient computational frameworks that combine advanced numerical methods with optimization algorithms from computer science has become essential. Pártl and Meneses Rioseco (2025a) and Pártl and Meneses Rioseco (2025b) proposed a novel computational framework that integrates non-matching discretization techniques, immersed boundary methods, and flux correction strategies with optimization algorithms to efficiently determine optimal multi-well configurations in three-dimensional fractured reservoirs. This approach enables evaluation of alternative well layouts within acceptable computational time, without repeated remeshing, thereby significantly reducing computational cost while preserving physical accuracy.

The development of such computational frameworks remains an ongoing effort. In this work, we present recent methodological advances with a particular focus on fracture–well intersections and the resulting flow and heat-transfer calculations. In addition, we provide further validation and verification of the numerical framework using benchmark and synthetic test cases. Special emphasis is placed on the practically relevant question of identifying the optimal inclination and azimuth of geothermal wells intersecting fracture-controlled reservoirs. In such systems, well orientation plays a decisive role in maximizing fracture intersections, enhancing effective well–reservoir connectivity, and ultimately increasing sustainable geothermal energy extraction. We present our most recent progress toward addressing these challenges and discuss implications for the optimization of geothermal reservoir performance.

2. Mathematical Model

Our mathematical model is based on those by Blank et al. (2021) and Zinsalo et al. (2020). It was already introduced by Pártl and Meneses Rioseco (2025a), where it is described in more detail, and tested further by Pártl and Meneses Rioseco (2025b).

We model the reservoir as a domain $\Omega \subset \boldsymbol{R}^3$consisting of 3D porous layers, Ω_{la}, porous fractures, Ω_{fr}(where $\Omega_{fr} \subset \partial\Omega_{la}$), and wells. The fractures are modeled as 2D manifolds with polygonal boundaries, and the wells are considered thin cylinders. As the radii of these cylinders are at least four orders of magnitude smaller than the dimensions of Ω_{la}, we include the wells into the model via the immersed boundary method (Peskin (2002) and Blank et al. (2021)). That is, we assume that the wells are not present in the domain, and we compensate for their absence by including special line mass and energy sources/sinks in the respective locations.

The reservoir is assumed to be non-deformable and fully saturated with a single-phase incompressible Newtonian fluid that is in local thermal equilibrium with the surrounding rock, where the rock is considered isotropic and heterogeneous. The aforementioned fluid is our model for water.

In the following sections, we use the subscripts *la*, *fr*, *r*, and *w* to distinguish between the objects associated with the layers, fractures, porous rock, and wells, respectively, whenever there may be confusion. The objects related to the fluid do not have any subscripts. The vectors and matrices are printed in boldface. The x, y, and z-component of a vector v are indicated by a regular font and the corresponding subscript, i.e., $v = (v_x, v_y, v_z)$.

2.1 Balance Equations

The fluid flow and heat transport in the reservoir are modeled by solving the corresponding balance equations for mass and energy while expressing the momentum balance via the Darcy law. In Ω_{la}, the equations are the following:

$$\varepsilon_r \frac{\partial \rho}{\partial t} + \nabla \cdot (\rho v) = S_{MW} \tag{1}$$

$$v = -\frac{1}{\mu} k(\nabla p - \rho g) \tag{2}$$

$$(\rho c_p)_{eff} \frac{\partial T}{\partial t} + \rho c_p v \cdot \nabla T - \nabla \cdot (\lambda_{eff} \nabla T) = S_{EW} \tag{3}$$

In Equation (1), ε_r [-] denotes the porosity, ρ [kg·m^{-3}] is the fluid density, t [s] represents the time, $\boldsymbol{v}$ [m/s] is the fluid velocity, and S_{MW} [kg·m^{-3}·s^{-1}] is the sum of the mass sinks/sources due to the wells.

In Equation (2), μ [Pa·s] stands for the dynamic viscosity of the fluid, and $\boldsymbol{k}$ [m^2] is the permeability tensor of the rock, where it holds $k = k \cdot I$ for a scalar function k [m^2] and the identity tensor $\boldsymbol{I}$. The symbol p [Pa] is the fluid pressure, and $\boldsymbol{g}$ [m/s^2] denotes the gravitational acceleration vector.

In Equation (3), c_p [J·kg^{-1}·K^{-1}] stands for the specific heat at constant pressure of the fluid, T [K] represents the common thermodynamical temperature of the fluid and rock, and S_{EM} [J·m^{-3}·s^{-1}] is the sum of the energy sinks/sources due to the wells. The subscript *eff* denotes the following combinations of the properties of the fluid and rock:

$$\lambda_{eff} = (1 - \varepsilon_r)\lambda_r + \varepsilon_r \lambda, \qquad (\rho c_p)_{eff} = (1 - \varepsilon_r)\rho_r c_r + \varepsilon_r \rho c_p$$

In the above formulas, ρ_r [kg·m^{-3}] is the density of the rock, c_r [J·kg^{-1}·K^{-1}] stands for the specific heat of the rock, and λ [W·m^{-1}·K^{-1}] represents the thermal conductivity coefficient.

In Ω_{fr}, we use the following system of equations:

$$d_{fr}\,\varepsilon_r \frac{\partial \rho}{\partial t} + d_{fr}\,\nabla_t \cdot\,(\rho v) = S_{MW} + (\rho v)^{+}_{la} \cdot\, n^{+} + (\rho v)^{-}_{la} \cdot\, n^{-} \tag{4}$$

$$v = -\frac{1}{\mu} k(\nabla_t p - \rho g_t) \tag{5}$$

$$d_{fr}\,(\rho c_p)_{eff} \frac{\partial T}{\partial t} + d_{fr}\,\rho c_p v \,\cdot\, \nabla_t T - d_{fr} \cdot\, \nabla_t(\lambda_{eff} \nabla_t T) = S_{EW} + q^{+}_{la} \cdot\, n^{+} + q^{-}_{la} \cdot\, n^{-} \tag{6}$$

for $q = -\lambda_{eff} \nabla T$.

In Equations (4)-(6), d_{fr} [m] denotes the fracture aperture, which we consider piecewise constant, and the operator ∇_t is the divergence/gradient in the direction tangential to the corresponding fracture. For a scalar-valued function f and a vector-valued function $\boldsymbol{f}$, it holds

$$\nabla_t f = \nabla f - (\nabla f \,\cdot\, n^{+}) \,\cdot\, n^{+}$$

$$\nabla_t \cdot f = (I - n^{+} \otimes\, n^{+}) : \nabla f$$

The symbol $n^{\pm}$ denotes the unit outward normals to the fracture, where $n^{+} + n^{-} = 0$, and the terms $(\rho v)^{\pm}_{la} \cdot\, n^{\pm}$ and $q^{\pm}_{la} \cdot\, n^{\pm}$ in Equations (4) and (6) are the fluxes entering or leaving Ω_{fr} through $\partial\Omega_{la}$. In Equation (5), we have $g_t = g - (g \,\cdot\, n^{+}) \,\cdot\, n^{+}$. Note that the units of the sinks/sources S_{MW} and S_{EW} in Equations (4) and (6) are kg·m^{-2}·s^{-1} and J·m^{-2}·s^{-1}, although they are denoted by the same symbols as the sinks/sources in Equations (1) and (3).

As for intersections of fractures, we consider only DFNs in which every intersection of N fractures is a line segment. Using the symbol $n^{s}_{\partial i}$ to denote the unit outward normal corresponding to the side $s \in \{+, -\}$ of such an intersection inside the i-th fracture, we prescribe

$$\sum_{i \in \{1,\dots,N\}} \sum_{s \in \{+,-\}} d_{fr,i} (\rho v)^{s}_{fr} \cdot n^{s}_{\partial i} = 0$$

$$\sum_{i \in \{1,\dots,N\}} \sum_{s \in \{+,-\}} d_{fr,i} q^{s}_{fr} \cdot n^{s}_{\partial i} = 0$$

We assume that p and T are continuous at the interface between the layers and the fractures, i.e., $p_{la}|_{\overline{\Omega_{fr}}} = p_{fr}$ and $T_{la}|_{\overline{\Omega_{fr}}} = T_{fr}$. This assumption together with the terms $(\rho v)^{\pm}_{la} \cdot\, n^{\pm}$ and $q^{\pm}_{la} \cdot\, n^{\pm}$ in Equations (4) and (6) assure the transfer of information between Ω_{fr} and Ω_{la}.

As for the boundary conditions, we prescribe the Dirichlet boundary conditions for p and T and $\rho v \cdot n = q_M$ and $q \cdot n = q_E$. We consider $q_M = 0$ and $q_E = 0$ on the whole of $\partial\Omega_{fr}$.

We solve the balance equations on the time interval $[t_{ini}, t_{fin}]$, where the primary variables are p and T. The corresponding initial conditions will be denoted by p_{ini} and T_{ini}. As for the parameters of the porous layers and fractures, we consider them constant in Ω_{la} and Ω_{fr} in this paper. We also consider the fluid properties constant in this paper.

2.2 Sinks and Sources Due to Wells

This section described how the wells are incorporated into the above balance equations. Each well w is cylindrical, and it is characterized by its type (an injection well acting as a source or a production well acting as a sink), position and orientation in space, height H_w [m], radius r_w [m], pump efficiency ε_w [-], and flow rate Q_w [m^3/s]. The injection well has a positive flow rate, and the production well has a negative flow rate. The fluid inside the well is characterized by its density ρ_w [kg·m^{-3}], temperature T_w [K], and specific heat capacity at constant pressure $c_{p,w}$ [J·kg^{-1}·K^{-1}].

Given non-empty sets of injection and production wells $\mathcal{W}_{inj}$ and $\mathcal{W}_{pro}$, respectively, the sinks/sources due to wells in Equations (1), (3), (4), and (6) are defined as follows:

$$S_{MW} = \sum_{w \in \mathcal{W}_{inj} \cup \mathcal{W}_{pro}} \rho_w C_w \delta_w$$

$$S_{EW} = C_{pen} \sum_{w \in \mathcal{W}_{inj} \cup \mathcal{W}_{pro}} \rho_w c_{p,w} C_w (T_w - T) \delta_w$$

In the above formulas, δ_w [m^{-2}] represents the Dirac delta function, and the terms C_w (where the physical unit is m^2/s in Ω_{la} and m^3/s in Ω_{fr}) depend only on the shape of the well w, its flow rate Q_w and the structure of the surrounding fractured porous medium. Through S_{EW}, we prescribe $T \coloneqq T_w$ in the well location via a penalty method, where C_{pen} [-] is a positive penalty parameter.

2.3 Optimization

For a given reservoir, time interval $[t_{ini}, t_{fin}]$, and given sets of wells $\mathcal{W}_{inj}$ and $\mathcal{W}_{pro}$ with variable positions inside the reservoir, we define the power P [W] of the geothermal facility as follows:

$$P = \frac{1}{t_{fin}-t_{ini}} \int_{t_{ini}}^{t_{fin}} \left(E_{pro}(t) - E_{pump}(t)\right) \mathrm{d}t \tag{7}$$

$$E_{pro}(t) = \sum_{w \in \mathcal{W}_{pro}} \left(\rho c_p T\right)\big|_w(t) \cdot |Q_w| - \sum_{w \in \mathcal{W}_{inj}} \rho_w c_{p,w} T_w Q_w \tag{8}$$

$$E_{pump}(t) = \sum_{w \in \mathcal{W}_{inj} \cup \mathcal{W}_{pro}} \frac{|Q_w|}{\varepsilon_w} \left| \triangle p \big|_w(t) \right| \tag{9}$$

In these formulas, E_{pro} [J/s] is the difference between the energy pumped out of and into the fractured rock through the wells, and E_{pump} [J/s] stands for the energy needed for the operation of the pumps. The parameter ε_w [-] is the pump efficiency, and $\triangle p \big|_w$ [Pa] is the average of $p - p_{ini}$ over the well.

We consider the optimal placement of these wells to be the one maximizing P over all admissible positions.

3. Numerical Solution

In this section, we briefly summarize how we solve the balance equations and optimization problem numerically. Our procedures are described in detail by Pártl and Meneses Rioseco (2025a).

The sinks/sources due to wells are approximated using the non-matching approach (see Peskin (2002) and Blank et al. (2021)) with an artificial extension of the well, w_ε, with an artificial well radius of $r_{\varepsilon,w}$ [m] ($r_{\varepsilon,w} \gg r_w$) to avoid the necessity of re-meshing the reservoir when changing the positions of the wells. We assume that a well intersects a fracture if the line segment connecting the centers of the well bases intersects this fracture.

We consider the following two approximations of the delta function δ_w for a well-fracture intersection:

i) The approximation used by Pártl and Meneses Rioseco (2025a) and Pártl and Meneses Rioseco (2025b). That is,

$$\delta_w(x) \approx \frac{\pi}{L_{\varepsilon,1} L_{\varepsilon,2} (\pi^2 - 4)} \theta\left(\frac{||x - C_\odot||_\odot}{\sqrt{L_{\varepsilon,1} L_{\varepsilon,2}}}\right) I_\odot(x)$$

$\theta(x) = cos(\pi x) + 1$ for $x < 1$, $\theta(x) = 0$ for $x \geq 1$

$$||x||_\odot = \sqrt{\frac{L_{\varepsilon,2}^2 |x_1|^2 + L_{\varepsilon,1}^2 |x_2|^2}{L_1 L_2}}$$

In the above definitions, we assume that the intersection of the plane in which the fracture lies and the well has a boundary in the form of an ellipse with the semi-major and semi-minor axes $L_{\varepsilon,1}$ and $L_{\varepsilon,2}$ [m], and a center $C_\odot$. The mapping $I_\odot: \Omega_{fr} \to \{0,1\}$ [-] is the indicator function of the interior and boundary of this ellipse, θ represents a cut-off function, and $||\cdot||_\odot$ is a norm related to the ellipse, where x_i is the i-th component of the point x expressed in the coordinate system given by $C_\odot$ and unit vectors pointing in the directions of the major and minor axes.

ii) The approximation $\delta_w \approx I_\otimes / A_\otimes$, where $I_\otimes: \Omega_{fr} \to \{0,1\}$ [-] is the indicator function of the intersection, and $A_\otimes$ [m^2] stands for the area of the intersection of the artificial extension of the well and the fracture.

The reason why we test the latter approximation of δ_w is that the first approximation introduces additional numerical error in cases where the ellipse does not lie fully inside the fracture.

Since each evaluation of the power P requires solving the balance equations on $[t_{ini}, t_{fin}]$, our primary aim was to devise a numerical scheme that could be implemented as a fast numerical solver. Therefore, we discretize the balance equations in time via a semi-implicit time-stepping scheme to avoid the solution of systems of nonlinear equations at each time step. The spatial discretization is based on the finite element method, employing P_1 elements both for p and T, and stabilizing the scheme using the algebraic flux correction with the Zalesak limiter (see Barrenechea et al. (2024) and Jha et al.(2023)). The resulting system of linear algebraic equations is solved via BiCGSTAB with the Jacobi preconditioning.

When evaluating the power P, the integral in Equation (7) is approximated using the trapezoidal rule, and the terms in Equations (8) and (9) evaluated at wells are approximated as weighted averages over the lateral surface of the well w. The optimization problem of

maximizing P is solved numerically employing the gradient-free global optimization algorithm AGS from the library NLopt by Johnson (2007).

As for the spatial meshes, we generate them using Gmsh and TetGen (see Geuzaine and Remacle (2009) and Si (2015)). Our numerical solver is implemented based on the library deal.II described by Africa et al. (2024).

4. Optimization Test

In this section, we describe two optimization tests that we performed using our numerical solver. The only difference between the tests is that in the first test, we use approximation i to approximate the delta function δ_w, and in the second test, we employ approximation ii. The test scenario is non-trivial but simplified enough for us to assess the plausibility of the results. To facilitate this assessment, we also use realistic values of physical parameters. The computer model of the DFN was created using the package Frackit by Gläser et al. (2020).

Unless otherwise stated, all physical quantities mentioned during our presentation are in the SI units, which corresponds to the units given in Sections 2 and 3.

4.1 Test Scenario

We consider $\overline{\Omega_{la}} = [-1200, 1400] \times [-1225, 1225] \times [-4250, -3900]$ and Ω_{fr} depicted in Figure 1. That is, Ω_{fr} consists of 12 square fractures with an edge length of 200 m, 11 of them being aligned in a stairs-like structure referred to as *stairs*. All fractures lie in the x-y-plane, and each of their edges is parallel either to the x-axis or to the y-axis. The barycenters of the fractures are $[-100, -125 + 25i, -4050 + 10i]$ for $i = 0, \ldots, 10$, and $[300, 0, -4001]$.

There are one injection well and one production well inside the reservoir. The injection well is vertical with its barycenter at $[300, 0, -4001]$ and a height H_w of 20 m. As for the production well, it has a height H_w of 280 m, the center of its upper base is at $[-100, y, -3945]$ for $y \in [-212.5, 212.5]$, and its direction is $(0, \sin\theta, \cos\theta)$ for $\theta \in [\frac{11\pi}{18}, \frac{25\pi}{18}]$. That is, the position and inclination of the production well can vary, the variables y and θ being our optimization parameters.

The values of the constant parameters introduced in Sections 2 and 3 are listed in Table 1. The initial condition for p and T are the following:

$$p_{ini}(x, y, z) = 101325 + \rho g_z z$$

$$T_{ini}(x, y, z) = 283.16 - 0.03 \cdot z$$

On the lateral boundaries of $\partial\Omega_{la}$, we prescribe the Dirichlet boundary conditions for p and T that equal the initial conditions. On the rest of $\partial\Omega_{la}$ and on $\partial\Omega_{fr}$, we prescribe $q_M = 0$ and $q_E = 0$. The operation of the wells in the reservoir is simulated for $t_{ini} = 0$ s, and $t_{fin} = 60 \cdot 60 \cdot 24 \cdot 365 \cdot 50$ s ≈ 50 years.

Table 1: Values of constant parameters introduced in Sections 2 and 3. The values of the fractured rock parameters correspond to the real ones, see, e.g., Frey et al. (2022), Narr et al. (2006), and Vidal et al. (2018). The fluid parameter values correspond to those of water at a temperature of 403.16 K, see Kretzschmar and Wagner (2014).

Parameter	Value	Unit	Parameter	Value	Unit	Parameter	Value	Unit
$\varepsilon_{r,la}$	0.1	-	ρ_r	2730.0	kg·m^{-3}	Q_w	±0.005	m^3·s^{-1}
$\varepsilon_{r,fr}$	0.03	-	c_r	2230.0	J·kg·K^{-1}	T_w	333.16	K
ρ	954.20	kg·m^{-3}	c_p	4169.7	J·kg·K^{-1}	$c_{p,w}$	4169.7	J·kg·K^{-1}
μ	2.23·10^{-4}	Pa·s	λ_r	4.07	W·m^{-1}·K^{-1}	r_w	0.07	m
k_{la}	3.0·10^{-16}	m^2	λ	0.71	W·m^{-1}·K^{-1}	C_{pen}	10^3	-
k_{fr}	2.083·10^{-9}	m^2	d_{fr}	2.0·10^{-4}	m	ε_w	0.6	-
g_z	-9.81	m·s^{-2}	ρ_w	954.20	kg·m^{-3}	$r_{\varepsilon,w}$	7.0	m

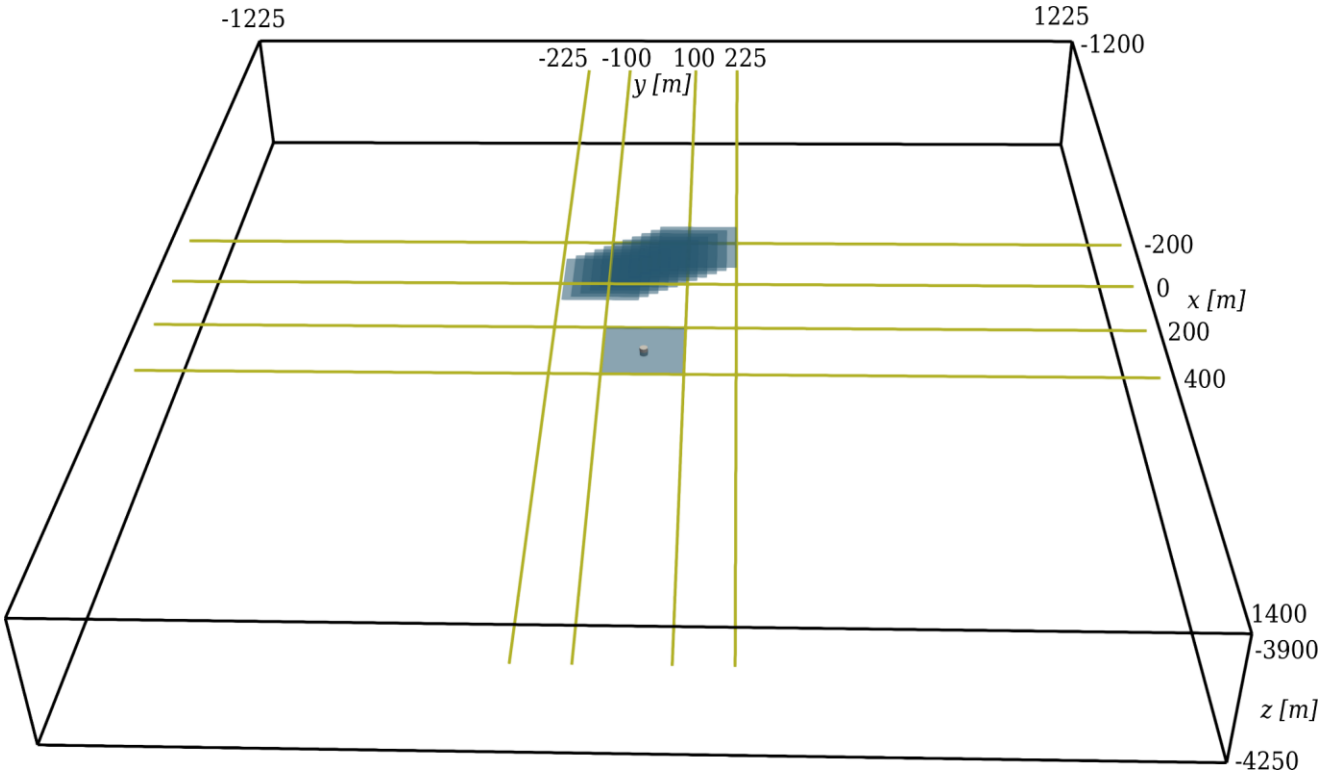

Figure 1: Ω_{la} and Ω_{fr} used in the tests. There are 11 square fractures aligned in a stairs-like structure and one single fracture. The gray cylinder inside the single fracture indicates the position of the injection well.

The mesh covering Ω_{la} consists of 3,157,002 tetrahedra, where the lengths of their edges are in $[1.4, 196.7\ ]$. The mesh covering Ω_{fr} consists of 229,229 triangles, where each triangle is a face of two tetrahedra, and each fracture is covered with triangles of approximately the same size. The edge lengths of the triangles are in $[1.4, 3.9]$. The time step for the approximation of the integral in Equation (7) and for the solution of the balance equations is $(t_{fin} - t_{ini})/50 \approx 1$ year.

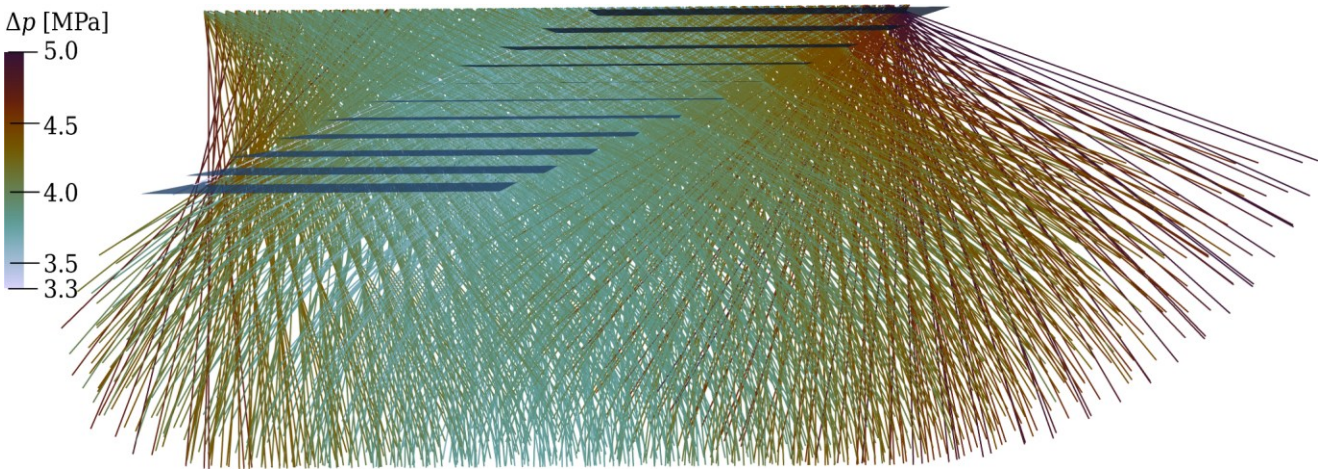

Figure 2: Positions of the production well tested during the optimization with approximation i of δ_w. Each well is represented by the line segment connecting the centers of its bases. The colors correspond to the sum of the pressure differences $\sum_{w \in \mathcal{W}_{inj} \cup \mathcal{W}_{pro}} |\triangle p|_w(t)|$ denoted by $\triangle p$.

4.2 Expected Results

Our test scenario is similar to those of the tests reported by Pártl and Meneses Rioseco (2025a) and by Pártl and Meneses Rioseco (2025b). However, varying the horizontal position and inclination of the production well means that the corresponding well-fracture intersections can be of various shapes, which adds a new level of complexity to the optimization problem. One intersection can be better than two intersections, for example.

Due to the similarity to the aforementioned tests, we expect the sum of pressure differences, $\sum_{w\in\mathcal{W}_{inj}\cup\mathcal{W}_{pro}} \left|\triangle p\right|_w(t)\left|\right.$, in Equation (9) to be a decreasing function of the number of fractures intersected by the production well if all corresponding intersections are of the same shape. We also expect this pressure difference to be minimum for a production well intersecting all 11 fractures forming the stairs. However, since the stairs are located 50 m below the top boundary of $\overline{\Omega_{la}}$ but 200 m above the bottom boundary of $\overline{\Omega_{la}}$, we expect the well-fracture intersections located deeper in Ω_{la} to lead to slightly lower pressure difference because there is more space from which the fluid can be pumped out around these intersections.

Due to the aforementioned similarity, we also expect the power P to be maximal for a production well intersecting only several of the lowermost fractures because the production temperature should be an increasing function of the average depth at which the well-fracture intersections are located.

4.3 Results

Figures 2-5 depict the results after 1500 optimization steps.

Figures 2 and 3 show the tested positions of the production well and indicate the corresponding sums of pressure differences, $\sum_{w\in\mathcal{W}_{inj}\cup\mathcal{W}_{pro}} \left|\triangle p\right|_w(t)\left|\right.$. We can see that the results for approximation ii match our expectations. In case of approximation i, however, we can see that the whitish wells are located along the left-hand edges of the stairs. That is, the very least sums of pressure differences were attained for wells that intersected the edges of the fractures, which represents the situation in which approximation i creates additional numerical error. Both figures indicate that the optimization algorithm searched approximately the whole parametric space without being trapped in one of its parts, which we consider favorable for the optimization.

Figures 4 and 5 show the wells for which the least sum of pressure differences, $\sum_{w\in\mathcal{W}_{inj}\cup\mathcal{W}_{pro}} \left|\triangle p\right|_w(t)\left|\right.$, and the highest power P were attained. The results for approximation ii meet our expectations: The sum of the pressure differences is the lowest for wells intersecting all 11 fractures, which are all the green wells except for the leftmost one. The leftmost one intersects only 10 fractures, and the corresponding sum of pressure differences is the highest of all green wells. The power P is the highest for the wells intersecting only 1 or 2 lowermost fractures, the best well intersecting only the lowermost fracture.

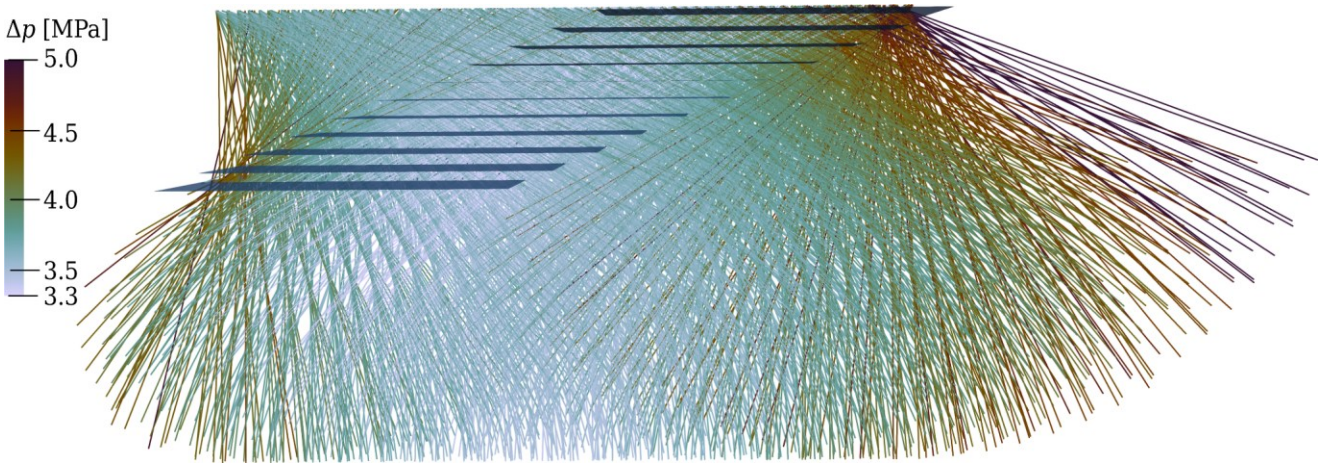

Figure 3: Positions of the production well tested during the optimization with approximation ii of δ_w. Each well is represented by the line segment connecting the centers of its bases. The colors correspond to the sum of the pressure differences, $\sum_{w\in\mathcal{W}_{inj}\cup\mathcal{W}_{pro}} \left|\triangle p\right|_w(t)\left|\right.$, denoted by $\triangle p$.

The results for approximation i seem to be affected by the above additional numerical error. As for the sum of pressure differences, we can see that only half of the orange wells displayed in Figure 4 intersect all 11 fractures. The other half of the orange wells intersect several fractures near their edges. The power P is the highest for wells intersecting several of the lowermost fractures, which meets our expectations, where the best well intersects 3 lowermost fractures. However, all of the displayed orange wells intersect some of the fractures near their edges, which could affect the results. The rightmost orange well intersecting 5 lowermost fractures probably belongs in the group of the very best wells only because of the aforementioned error.

Note that for each approximation of δ_w, the optimum number of intersected lowermost fractures may be different because these approximations yield slightly different pressure and temperature distributions. Therefore, we generally do not consider differences in the number of lowermost fractures intersected by the best wells to be incorrect. Also note that the values of the power P are low because the well flow rate Q_w is merely 0.005 $m^3 \cdot s^{-1}$.

5. Conclusions

In this contribution, we presented recent developments and numerical results obtained with a computational framework for the optimization of geothermal well configurations in fracture-controlled reservoirs. The framework combines discrete fracture network modeling with non-matching discretization and immersed boundary techniques, enabling efficient evaluation of different well placements without repeated remeshing. The focus of this work was placed on the numerical treatment of well–fracture intersections and on the influence of production well inclination and azimuth on reservoir performance.

Two alternative approaches for modeling well–fracture intersections were investigated and assessed within an optimization setting. The results demonstrate that the choice of the intersection treatment has a significant impact on the pressure response, thermal performance, and robustness of the optimization outcome. In particular, approximation i of well–fracture intersections was found to reduce numerical artifacts associated with edge intersections and to yield results that are more consistent with physical expectations for fracture-controlled flow and heat transport.

The conducted optimization tests confirm that production well orientation strongly affects both hydraulic connectivity and thermal power output in fractured reservoirs. While intersecting a larger number of fractures generally reduces pressure losses, the optimal thermal performance is achieved for well positions intersecting a limited number of deeper fractures, highlighting the trade-off between hydraulic efficiency and thermal depletion. These findings emphasize the importance of explicitly accounting for fracture geometry and well–fracture interaction when optimizing well positions in fractured geothermal systems.

Overall, the presented results provide further verification and validation of the proposed computational framework and demonstrate its capability to reliably capture the effects of well orientation and well–fracture geometry in complex fractured reservoirs. The developed methodology represents a step toward computationally efficient and physically consistent optimization workflows and provides a basis for future studies addressing more complex fracture networks, multi-well configurations, and application-oriented geothermal reservoir scenarios.

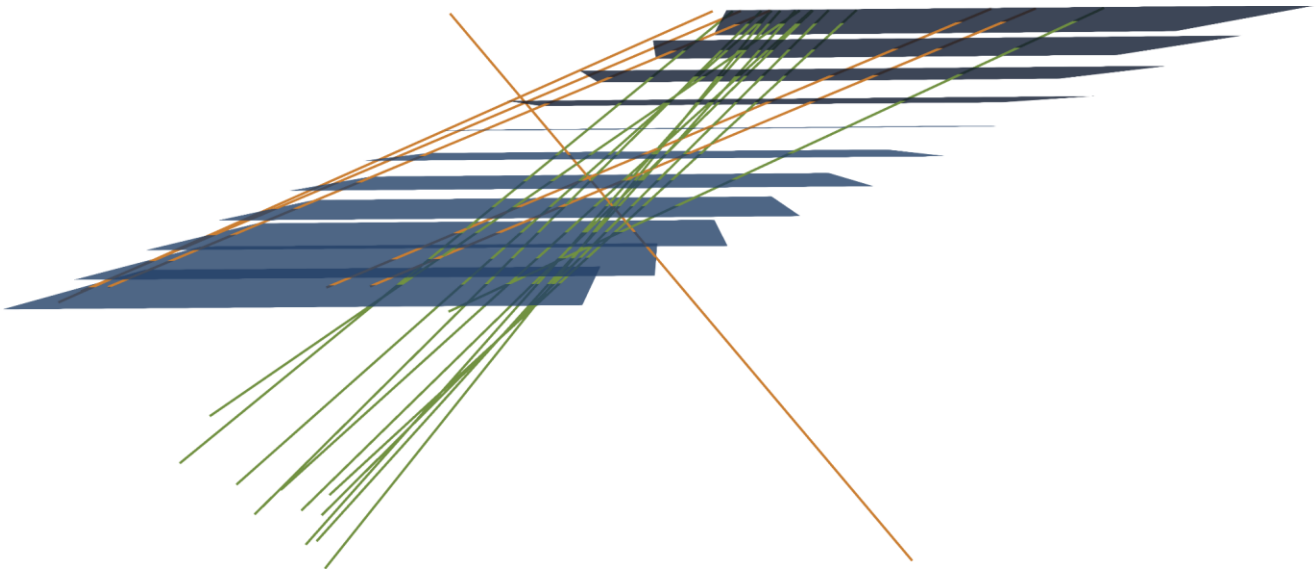

Figure 4: Positions of the production well with the lowest sums of pressure differences, $\triangle p = \sum_{w \in \mathcal{W}_{inj} \cup \mathcal{W}_{pro}} |\triangle p|_w(t)|$, during the tests with approximation i (orange) and ii (green) of δ_w. Each well is represented by the line segment connecting the centers of its bases. The orange wells are those for which we have $\triangle \boldsymbol{p} \in [3.3, 3.55]$ in MPa. The green wells are all wells for which it holds $\triangle \boldsymbol{p} \in [3.56, 3.58]$ in MPa. In both cases, the lower bound of the interval is the minimum $\triangle \boldsymbol{p}$.

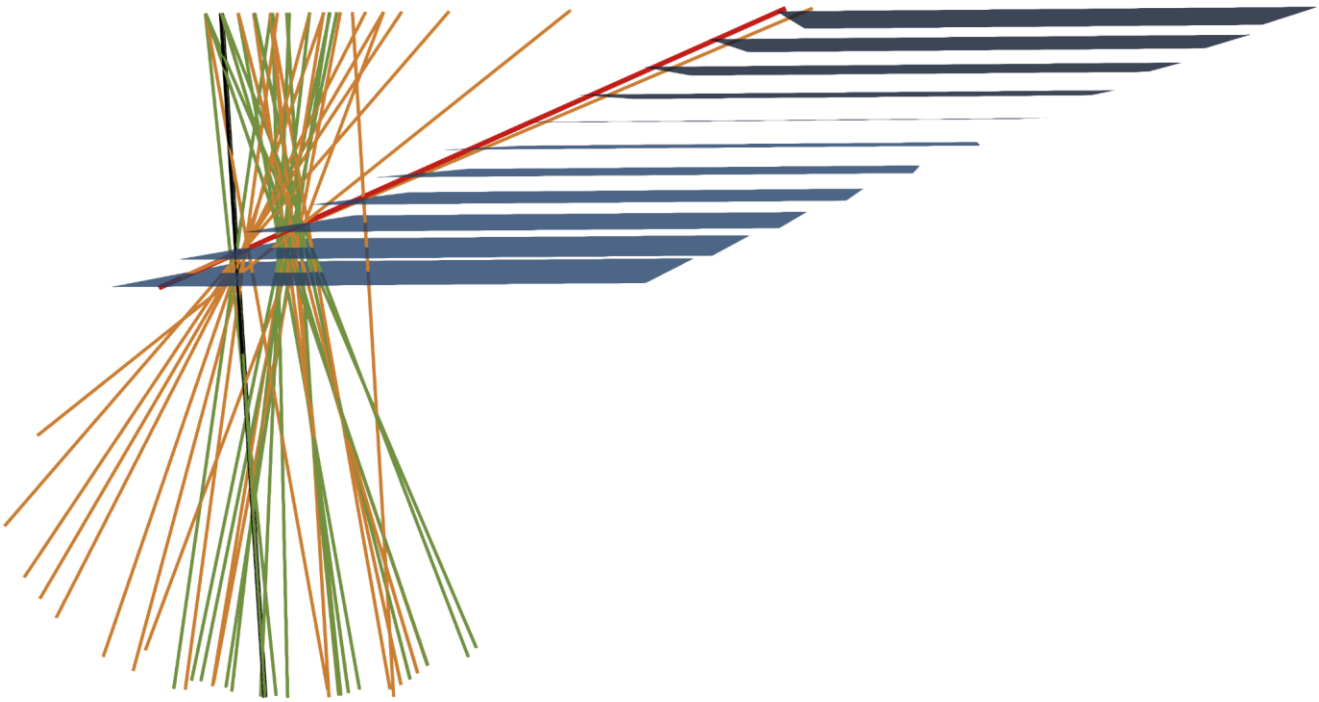

Figure 5: Positions of the production well that yielded the highest power P during the tests with the approximation i (orange) and ii (green) of δ_w. Each well is represented by the line segment connecting the centers of its bases. The orange wells are those for which we have $\boldsymbol{P} \in [\mathbf{1.32}, \mathbf{1.325}]$ in MW. The best of these wells, which intersects three lowermost fractures, is in red. The green wells are all wells for which it holds $\boldsymbol{P} \in [\mathbf{1.32}, \mathbf{1.321}]$ in MW, the optimum well being in black. The optimum well intersects only the lowermost fracture.

REFERENCES

Africa, P.C., Arndt, D., Bangerth, W., et al.: The deal.II library, Version 9.6, Journal of Numerical Mathematics, (2024), 32(4):369–380.

Barenblatt, G.E., Zheltov, I.P., and Kochina, I.N.: Basic concepts in the theory of homogeneous liquids in fissured rocks. Journal of Applied Mathematics and Mechanics, (1960), 24(5): 1286–1303.

Barrenechea, G.R., John, V., Knobloch, P.: Finite Element Methods Respecting the Discrete Maximum Principle for Convection-Diffusion Equations, SIAM Review , (2024), 66(1):3-88.

Bauer, J.F., Meier, S., and Philipp, S.L.: Architecture, fracture system, mechanical properties and permeability structure of a fault zone in Lower Triassic sandstone, Upper Rhine Graben. Tectonophysics, (2015), 647–648: 132–145.

Berre, I., Doster, F., and Keilegavlen, E.: Flow in fractured porous media: A review of conceptual models and discretization approaches. Transport in Porous Media, (2019), 130: 215–236.

Blank, L., Meneses Rioseco, E., Caiazzo, A., Wilbrandt, U.: Modeling,simulation, and optimization of geothermal energy production from hot sedimentary aquifers, Computational Geosciences, (2021), 25:67–104.

Bödvarsson, G.S., and Tsang, C.F.: Injection and thermal breakthrough in fractured geothermal reservoirs. Journal of Geophysical Research: Solid Earth, (1982), 87(B2): 1031–1048.

Bratton, T., Canh, D.V., Que, N.V., Duc, N.V., Gillespie, P., Hunt, D., Li, B., Marcinew, R., Ray, S., Montaron, B., Nelson, R., Schoderbek, D., and Sonneland, L.: The nature of naturally fractured reservoirs. Oilfield Review, 2006, 18(2): 4–23.

Cao, M., and Sharma, M.M.**:** Impact of well placement on heat production from complex fracture networks in enhanced geothermal systems: A semi-analytical model. Geoenergy Science and Engineering, (2024), 234: 212693.

Dussel, M., Lüschen, E., Thomas, R., Agemar, T., Fritzer, T., Sieblitz, S., Huber, B., Birner, J., and Schulz, R.: Forecast for thermal water use from Upper Jurassic carbonates in the Munich region (South German Molasse Basin). Geothermics, (2016), 60: 13–30.

Fadel, M., Meneses Rioseco, E., Bruna, P.O., and Moeck, I.: Pressure transient analysis to investigate a coupled fracture corridor and a fault damage zone causing an early thermal breakthrough in the North Alpine Foreland Basin. Geoenergy Science and Engineering, (2023), 229: 212072.

Frey, M., Bär, K., Stober, I., Reinecker, J., van der Vaart, J., and Sass, I.: Assessment of deep geothermal research and development in the Upper Rhine Graben. Geothermal Energy, (2022), 10:18.

Gan, Q., and Elsworth, D.: Production optimization in fractured geothermal reservoirs by coupled discrete fracture network modeling. Geothermics, 2016, 62: 131–142.

Geuzaine, C., Remacle, J.F.: Gmsh: A 3-D finite element mesh generator with built-in pre- and post-processing facilities, International Journal for Numerical Methods in Engineering, (2009), 79(11):1309-1331.

Glaas, C., Vidal, J., and Genter, A.: Structural characterization of naturally fractured geothermal reservoirs in the central Upper Rhine Graben. Journal of Structural Geology, (2021), 148: 104370.

Gläser, D., Flemisch, B., Class, H.,Helmig, R.: Frackit: a framework for stochastic fracture network generation and analysis, Journal of Open Source Software, (2020), 5:2291.

Gringarten, A.C.: Flow-test evaluation of fractured reservoirs. In: Narasimhan, T.N. (ed.), Recent trends in hydrogeology, Geological Society of America Special Paper 189, (1982), Geological Society of America, Boulder, Colorado, USA, 237–258.

Jha, A., Pártl, O., Ahmed, N., Kuzmin, D.: An assessment of solvers for algebraically stabilized discretizations of convection–diffusion–reaction equations, Journal of Numerical Mathematics, (2023), 31(2):79–103.

Johnson, S.G.: The NLopt nonlinear-optimization package., https://github.com/stevengj/nlopt, (2007).

Kretzschmar, H.J., Wagner, W.: International Steam Tables: Properties of water and steam based on the industrial formulation IAPWS-IF97, Springer Berlin, Heidelberg, (2014).

Krumbholz, J.F., Krumbholz, M., Wadas, S.H., and Tanner, D.C.: Characterisation of the fracture- and karst-controlled geothermal reservoir below Munich from geophysical wireline and well information. Geothermal Energy, (2024) , 12: 9.

Long, J.C.S., and Witherspoon, P.A.: The relationship of the degree of interconnection to permeability in fracture networks. Journal of Geophysical Research: Solid Earth, (1985), 90(B4), 3087–3098.

Moinfar, A., Varavei, A., Sepehrnoori, K., and Johns, R.T.: Development of an efficient embedded discrete fracture model for 3D compositional reservoir simulation in fractured reservoirs. SPE Journal, (2014), 19: 289–303.

Narr, W., Schechter, D.S., and Thompson, L.B.: Naturally fractured reservoir characterization. Society of Petroleum Engineers, (2006), Richardson, Texas, USA.

Pártl, O., Meneses Rioseco, E.: Efficient numerical framework for geothermal energy production optimization in fracture-controlled reservoirs, International Journal for Numerical Methods in Fluids, xx, (2025a), xx-xx.

Pártl, O., Meneses Rioseco, E.: Geothermal well placement optimization for sustainable energy production: New computational framework for fracture-controlled reservoirs, Proceedings, European Geothermal Congress 2025, Federal Institute of Technology Zurich, Switzerland, (2025b).

Patterson, J.R., Cardiff, M., and Feigl, K.L.: Optimizing geothermal production in fractured rock reservoirs under uncertainty. Geothermics, (2020), 88: 101906.

Peskin, C.S.: The immersed boundary method, Acta Numerica, (2002), 11:479–517.

Salimzadeh, S., Grandahl, M., Medetbekova, M., and Nick, H.M.: A novel radial jet drilling stimulation technique for enhancing heat recovery from fractured geothermal reservoirs. Renewable Energy, (2019), 139: 395–409.

Schulte, T., Zimmermann, G., Vuataz, F., Portier, S., Tischner, T., Junker, R., Jatho, R., and Huenges, E.: Enhancing geothermal reservoirs. In: Huenges, E. (ed.), Geothermal energy systems: Exploration, development, and utilization, Wiley-VCH Verlag GmbH & Co. KGaA, (2010), Weinheim, Germany, 173–243.

Sepehrnoori, K., Xu, Y., and Yu, W.: Embedded discrete fracture modeling and application in reservoir simulation. Developments in Petroleum Science, (2021), Vol. 68, Elsevier B.V., Amsterdam, The Netherlands.

Si, H.: TetGen, a Delaunay-Based Quality Tetrahedral Mesh Generator, ACM Transactions on Mathematical Software, (2015), 41(2).

Vidal, J., and Genter, A.: Overview of naturally permeable fractured reservoirs in the central and southern Upper Rhine Graben: Insights from geothermal wells. Geothermics, (2018), 74: 57–73.

Wang, Y., de Hoop, S., Voskov, D., Bruhn, D., and Bertotti, G.: Modeling of multiphase mass and heat transfer in fractured high-enthalpy geothermal systems with advanced discrete fracture methodology. Advances in Water Resources, (2021), 154: 103985.

Warren, J.E., and Root, P.J.: The behavior of naturally fractured reservoirs. SPE Journal, (1963), 3: 245–255.

Zinsalo, J.M., Lamarche, L., Raymond, J.: Injection strategies in an enhanced geothermal system based on discrete fractures model, Applied Thermal Engineering, 169, (2020), 114812.